Research Article Vol. 27, No. 20 / 30 September 2019 / Optics Express 29016

Optics EXPRESS

Optimised XUV holography using spatially shaped high harmonic beams

D. J. Treacher,[1,*] D. T. Lloyd,[1] F. Wiegandt,[1] K. O'Keeffe,[2] and S. M. Hooker[1]

[1] *Department of Physics, University of Oxford, Clarendon Laboratory, Parks Road, Oxford OX1 3PU, UK*
[2] *College of Science, Department of Physics, Swansea University, Singleton Park, Swansea SA2 8PP, UK*
[*] *daniel.treacher@physics.ox.ac.uk*

Abstract: We present a novel method for controlling the transverse positions and relative powers of multiple high-order harmonic beams. A phase-only spatial light modulator is used to produce multiple infrared foci, the positions and intensities of which can be controlled programmably, enabling the generation and control of multiple HHG beams. To demonstrate the utility of this method we perform Fourier transform holography with separate illumination of the object and reference pinhole by a pair of HHG beams, which makes optimal use of the available photon flux. The programmable control of the spatial distribution of HHG beams demonstrated here offers new opportunities for experiments at extreme ultraviolet (XUV) wavelengths, particularly for photon intensive applications such as imaging.

1. Introduction

High harmonic generation (HHG) driven by tabletop laser systems has emerged as an accessible method for generating coherent radiation in the vacuum ultraviolet (VUV) and soft x-ray (SXR) spectral regions [1]. The high spatial and temporal coherence of HHG sources coupled with their sub-femtosecond pulse durations has made HHG an attractive source for a range of applications including the real-time observation of ultrafast dynamics in gases [2] and solids [3], the metrology of quantum-tunnelling [4] and element and depth sensitive imaging [5,6].

Although HHG has proven to be a valuable tool for high temporal and spatial resolution imaging many applications are limited by the low conversion efficiency of infrared to harmonic photons. This typically restricts harmonic sources to μW or nW of average power [7,8]. Several approaches have been adopted to address this fundamental bottleneck, including the use of phase-matching [9], quasi-phase matching [10,11] and high-repetition rate driver lasers [12]. However, to date, little attention has been given to controlling the spatial properties of HHG beams, despite the fact that many applications, such as imaging, would benefit greatly from this degree of control. Control of the spatial distribution of HHG photons would allow the optimum use of the limited available flux, mitigating the low conversion efficiency.

The manipulation of XUV radiation is hindered by the complexity and inefficiency of available optics [13]. The limited efficiencies [14] of these narrowband optics have led to the use of hybrid lenses that combine diffraction and refraction [15,16], although their construction remains highly complex and expensive [17].

Shaping of XUV radiation has been demonstrated by splitting the fundamental beam to create multiple IR driver beams [18,19], although only limited control over the positions and relative powers of the XUV beams is possible with this approach. Alternatively an HHG beam can be divided by a split XUV mirror [20,21]. However, in this optomechanical approach, the number of independent harmonic beams is implicitly limited to the number of mirror facets.

#367511 https://doi.org/10.1364/OE.27.029016
Journal © 2019 Received 13 May 2019; revised 9 Aug 2019; accepted 29 Aug 2019; published 25 Sep 2019

Lensless Fourier transform holography (FTH) has emerged as a favoured application of HHG for obtaining near wavelength scale resolution images [22–24]. Its lensless nature and the simplicity of the analytic reconstruction process makes it very attractive to applications in the vacuum ultraviolet (VUV) and soft x-ray (SXR) regimes [25]. With a high harmonic beam of 18.1 nm wavelength, a spatial resolution of 34 nm has been reported [26] when FTH is combined with post processing phase retrieval algorithms [24,27,28].

In FTH, radiation transmitted by the object is interfered with a reference wave to form a hologram in the detection plane located behind the object. The reference wave is provided by the light transmitted through a reference aperture located in the object plane. In this case an inverse Fourier transform of the measured hologram yields the convolution of the reference and object. For a reference aperture much smaller than the object, such as a pinhole, this is equivalent to an image of the object that is located at the position of the reference pinhole. In order to prevent the recovered image being obscured by the on-axis autocorrelation, the reference pinhole should be separated from the centre of the object by at least 1.5 times the diameter of the object [29].

A common metric of image quality is the intensity contrast [30] between the image itself and the background, which is intrinsically linked [31] to its signal to noise ratio S:N = $\mu_{\text{sig}}/\sigma_{\text{bg}}$ [32]. Here μ_{sig} and σ_{bg} are the mean of the image signal and standard deviation of the background respectively. In the absence of noise and numerical artefacts, the contrast in the recovered FTH image is proportional to the visibility of the detected interference fringes. The fringe visibility is maximised when the amplitudes of the object and reference waves leaving the back of the sample are comparable [33]. When an absorptive object and transmissive reference feature are illuminated, an imbalance in the illuminating intensity may be required to ensure the amplitudes leaving the rear of both features are comparable. This may not be possible with the traditional single Gaussian illuminating beam.

The S:N of recovered FTH images can be further improved by averaging the images retrieved from several reference pinholes [34]. In the most commonly employed geometry, a single beam encompasses both the reference pinholes and the object, with the consequence that photons impinging upon opaque regions outside these features are lost and do not contribute to the detected signal.

In this article, we use a phase-only spatial light modulator (SLM) to produce multiple driver foci in a gas cell which subsequently generate multiple HHG beams. We present an experimental demonstration of the programmable control over the spatial distribution and relative powers of two HHG beams. We further demonstrate the use of these fully decoupled beams in an FTH experiment. When the two beams are spatially shaped to match the distribution of the object and reference features, the available harmonic flux is more efficiently utilised, with the additional advantage of the ability to adjust the distribution of energies in the illuminating beams. We demonstrate that the S:N of the image recovered with two independently controlled beams is superior to that of the image recovered with only one illuminating beam.

2. Experimental arrangement

A schematic diagram of the beamline used in this experiment is shown in Fig. 1(a). The driver pulses produced by a Ti:Sapphire regenerative amplifier (Spitfire Pro, Spectra Physics) were shaped by a liquid crystal on silicon (LCoS) SLM (model X10468-02, Hamamatsu). The active area comprised 792 x 600 square pixels of side 20 μm with a fill factor of 98%. During all experiments, a phase mask with the device calibration and residual aberration corrections was displayed on the SLM at all times. The shaped beam was focussed by a plano convex lens of focal length $f = 50$ cm into a nickel gas cell backed by $60 - 80$ mbar of argon. The fundamental beam had a central wavelength of 800 nm, a e^{-2} radius of $w = 4.3$ mm, a pulse repetition rate of 1 kHz, a pulse duration of 35 fs and a pulse energy of 1 mJ.

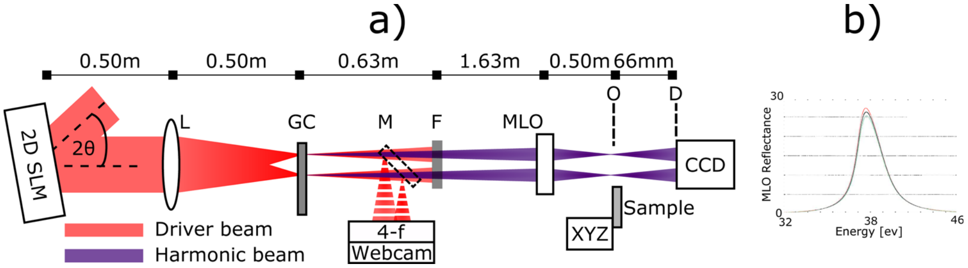

Fig. 1. a) Schematic diagram of the experimental beamline downstream of the SLM. The labels are as follows: SLM is the spatial light modulator, θ is the angle of incidence to the SLM which was <5°, L is the IR focusing lens, GC is the nickel gas cell and M is a mirror that when in place, deflects the driver beam onto a CCD through a 4-f unitary magnification reimaging line that allows inspection of the focal plane. F represents Aluminium filters, MLO represents a pair of multilayered XUV optics and XYZ represents a 3 axis optically encoded translation stage. The object and detection planes are denoted 'O' and 'D' respectively. b) Reflectance curve of both MLO.

The harmonics generated in the 900 μm thick gas cell propagated 0.63 m until they reached a pair of 400 nm thick aluminium filters (Sandwich filter, Lebow) with clear apertures of 10 mm diameter. These filters eliminated the IR radiation but transmitted the 13th to 46th harmonics with a varying degree of attenuation. Approximately 15% of the 25th harmonic order was transmitted [35], which subsequently reached the multilayered XUV optics 1.63 m farther downstream. These optics consisted of a B_4C/Si multilayer mirror, MLM, and a B_4C/Si multilayer focussing mirror, MLFM (Fraunhofer IWS) each of which reflected approximately 26% of the harmonic order used to illuminate the sample (25th harmonic with a central wavelength of 32 nm) with a bandwidth of 1.6 nm. The MLFM was designed for use at an angle of incidence of 7 degrees. Any deviation from this will introduce aberrations into the harmonic beam in addition to the astigmatism unavoidably caused by the off-axis illumination of the MLFM. The 25th harmonic was then reimaged by the MLFM of focal length $f = 50$ cm onto the sample in the object plane. The sample was mounted on an optically encoded XYZ stage (SLC-1780-S, SmarAct). The XUV radiation transmitted by the sample was recorded further downstream in the detector plane by a back illuminated CCD (iKon-L, ANDOR), comprising 2048 x 2048 square pixels of side 13.5 μm with a fill factor of 100%. During data acquisition, the chip was cooled to -45°C. The vacuum chambers housing the harmonic radiation were maintained at pressures below 10^{-3} mbar and that housing the CCD was held at 10^{-6} mbar.

3. Driver phase mask

To generate multiple IR foci the SLM displayed a phase mask comprising N contiguous annuli. Each annulus encoded a different phase gradient and each formed a focus at a position determined by the phase gradient in the annulus. It can be shown that the location $(\Delta X, \Delta Y)$ of each focus in the focal plane is governed by the magnitude and direction of the linear phase gradient $\dot{\phi}_{\text{trans}}$ placed on the beam [36] according to

$$\dot{\phi}_{\text{trans}} = \frac{2\pi}{\lambda f}\,(\Delta X x + \Delta Y y) \tag{1}$$

where λ is the wavelength, f is the focal length of the lens and x, y are the transverse coordinates in the SLM plane.

The radii of the annuli are initially calculated to ensure that each contains $1/N$ of the driver laser power. Assuming a Gaussian beam this requirement yields

$$\int_0^{2\pi}\int_{r_n}^{r_{n+1}} I_0\, \mathrm{e}^{-2\left(\frac{r}{w}\right)^2} r\,dr\,d\theta = \frac{1}{N}\int_0^{2\pi}\int_0^{\infty} I_0\, \mathrm{e}^{-2\left(\frac{r}{w}\right)^2} r\,dr\,d\theta. \tag{2}$$

where w is the e^{-2} radius of the beam, I_0 is the peak intensity, and r and θ are the radial and azimuthal coordinates in the SLM plane. Solving for r_{n+1} yields the recursion relation:

$$r_{n+1} = w \cdot \sqrt{\frac{1}{2}\,\log_{\mathrm{e}}\left[\frac{1}{\exp\{-2\left(\frac{r_n}{w}\right)^2\} - \frac{1}{N}}\right]}, \tag{3}$$

where $r_1 = 0$ mm. This enables the remaining zone radii to be calculated ensuring a theoretically equal distribution of driver power exists within each zone. In practice however, the zone radii were adjusted experimentally from initial values calculated from Eq. 3 to account for inhomogeneities of the incident beam. With this approach the spot size of the focus generated by each annulus will tend to decrease with n since $r_n > r_{n-1}$. To obtain foci of equal intensity the radii r_n can be iteratively optimised. Figure 2 shows an example phase mask and the experimentally measured focus the shaped beam produces, showing 7 spatially separated foci. The positions of these foci can be controlled by adjusting the phase gradients in accordance with Eq. 1.

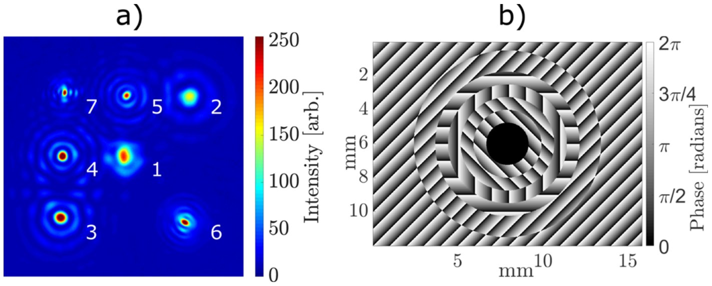

Fig. 2. a) Measured transverse intensity profile of the infrared radiation after transmission through the phase mask shown in b) and focusing by a $f = 50$ cm lens. The numbers shown next to the foci in a) indicate the corresponding annulus responsible for their creation in b), numbered in order of increasing annulus radius. Beams 6 and 7 in (a) are lacking in circular symmetry because the mask in (b) assumes a perfect incident Gaussian driver beam with no asymmetry, imperfections or clipping. This discrepancy could be accounted for using a priori information about the incident intensity profile.

4. Driver and harmonic beams

For the FTH demonstration, the driver focus was separated into $N = 2$ foci. The phase mask therefore comprised two zones: an inner zone of radius 3.3 mm and no phase shift; and an outer zone, comprising the remainder of the mask which displayed a linear phase gradient of $\dot{\phi}_{\mathrm{trans}} = 2356.2$ rad m^{-1} in $\hat{x}$ such that the first focus was on axis and the second was designed to be 150 μm off axis in $\hat{x}$. Figure 3(a) shows the transverse profile of the IR focus produced with this SLM mask, measured along the x-axis. Also shown are the corresponding simulated transverse profiles of the intensity and phase. These data show the separation of the two foci to be (146 ± 1) μm, which compares very well with the design separation of 150 μm.

The phase steps in Fig. 3(a) occur at points where the simulated intensity drops to zero. Across the two intensity peaks the simulated phase remains flat as desired. Angular spectrum method

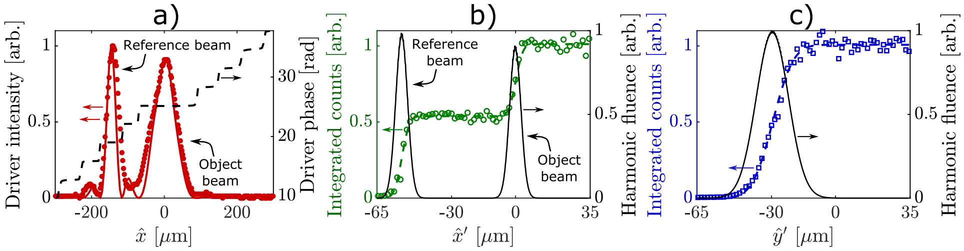

Fig. 3. a) Measured transverse intensity profile (red dots) in the driver focal plane ($\hat{x}$) of the IR focus produced by a $N = 2$ SLM mask with parameters given in the text. The simulated intensity (red, solid) and simulated phase (black, dashed) profiles are overlaid. b) Measured variation of the harmonic signal as a function of the position of a knife edge inserted in the beam with its edge parallel to $\hat{y}'$ coordinates in the harmonic focal plane shown by green points, along with the fit (dashed green line). Only every third data point is shown, however the fit was made to the complete dataset. The transverse fluence profile of the harmonic beam in the $\hat{x}'$ dimension (solid black line) was calculated by differentiating [37] the corresponding fit. c) Shows the counterpart data to (b) but in the perpendicular transverse dimension.

(ASM) simulations of the longitudinal evolution of the phase indicate that it remains circularly symmetric across the intensity peaks over a distance larger than the gas cell thickness.

Using 1 mJ of pulse energy, the driver focal intensity distribution shown in Fig. 3(a) was used to generate harmonics in a gas cell backed by 70 mbar of argon. In order to establish the spatial separation of the reimaged harmonic sources in $\hat{x}'$, the CCD signal was recorded as a function of the transverse position of a knife edge located 50 cm downstream of the MLFM. Figures 3(b) and 3(c) show the corresponding data and fit for knife edge translations in the $\hat{x}'$ and $\hat{y}'$ dimensions respectively. In both cases, the fits were made to the sum of two error functions [38]. Fitting to an error function assumes that the reimaged harmonic foci have Gaussian intensity profiles.

The green dashed curve in Fig. 3(b) reveals that (53 ± 0.5) % of the harmonic energy is located in the reference beam. The spot sizes in $\hat{x}'$ of the reference and object beams are (5.4 ± 0.7) μm and (4.9 ± 0.5) μm respectively. They are separated by (52.4 ± 0.5) μm, which is consistent with the propagation of the harmonic beams over the 2.27 m between the gas cell and the MLFM, and the demagnification of the MLFM. The scan along the $\hat{y}'$ dimension, shown in Fig. 3(c) reveals only one step, with a deduced spot size of (7.6 ± 1.3) μm. Taken together, the results show the formation of two harmonic beams with beam centres separated along the $\hat{x}'$-axis.

5. Fourier transform holography

To provide a proof-of-principle demonstration of optimized XUV holographic imaging, FTH was undertaken with two XUV beams generated by the method described above. The sample comprised a 200 x 200 x 0.05 μm silicon nitride (Si_3N_4) membrane supported within a 5 x 5 x

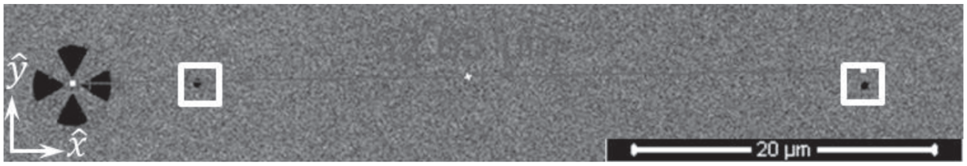

Fig. 4. Scanning electron microscope image of the FTH sample that comprises the object to the left and two reference holes outlined by white squares. The faint horizontal grey line is a ruler drawn on the SEM image in the focussed ion beam software.

0.525 mm silicon wafer (Silson Ltd). This was sputter coated with gold of 150 nm thickness. A pattern was then milled through both the gold and Si_3N_4 substrate with a gallium-based focussed ion beam (FEI company) to act as an object.

The object was accompanied by near and far reference holes. Reference holes were milled, laterally displaced from the object. The near reference was located at 8 μm in $\hat{x}$ from the object to satisfy the holographic separation condition. The far reference was located at 52.4 μm in $\hat{x}$ from the object matching the harmonic foci separation established above. An electron beam image of the sample is shown in Fig. 4.

6. Comparison

Our HHG beam shaping method allows the object and reference holes to be illuminated efficiently by a pair of beams with user defined relative intensities. This is not possible with unshaped illumination without moving the sample away from the focus, which wastes XUV flux. Ergo, for a fixed intensity of illumination, an experiment with shaped beams should provide images with a significantly higher S:N than obtained from their unshaped counterpart.

For a fair comparison, both the relative and absolute intensities illuminating the object and reference pinhole should be comparable for the $N = 1$ and $N = 2$ cases. Figure 5 illustrates the two cases schematically. In Fig. 5(a), the $N = 2$ case comprises spatially separate but mutually coherent object and reference beams. Their respective intensities at the object and far reference (R_2) are I_{obj} and I_{R_2}, with a ratio $\alpha_2 = \frac{I_{\mathrm{obj}}}{I_{R_2}}$.

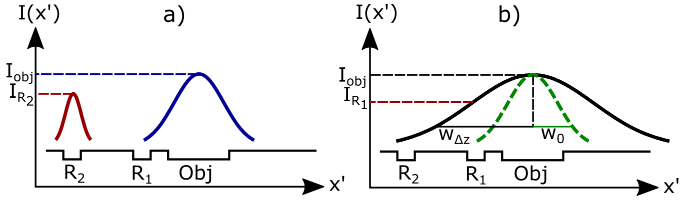

Fig. 5. Schematic illustrations of: a) Illumination of the object and reference hole R_2 by a pair of harmonic beams; and b) Illumination of the object and reference hole R_1 by a single beam. The labels 'Obj', R_1 and R_2 refer to the object, near reference and far reference respectively. More detail is in the text.

Figure 5(b) shows two cases corresponding to $N = 1$. For a single beam centred on the object (dashed curve) it is impossible to achieve $\alpha_1 = \alpha_2$, where $\alpha_1 = \frac{I_{\mathrm{obj}}}{I_{R_1}}$. However, by moving the object longitudinally a distance Δz away from the focus, it is possible to achieve $\alpha_1 \approx \alpha_2$. The spot size of the unshaped XUV beam required to give $\alpha_1 \approx \alpha_2$ is

$$w_{\Delta z} = \frac{d}{\sqrt{\frac{1}{2}\log_e\left(\frac{1}{\alpha}\right)}}, \tag{4}$$

where d is the fixed distance of 8 μm between the centres of the object and R_1. From Fig. 3(b), we have achieved $\alpha_2 = 0.88 \pm 0.02$ and hence $w_{\Delta z} = (31.6 \pm 0.2)$ μm is required for α_1 to match α_2.

The longitudinal movement of the sample required to fulfil this criteria was found experimentally to be $\Delta z = 2.5$ mm downstream of the unshaped harmonic focus. This shift reduced the minimum theoretically resolvable feature size from 76 nm to 73 nm [39]. With this shift the object is illuminated by a spherical wavefront when it is placed out of the harmonic focus; simulations suggest the effect this has on the recovered image is negligible.

The procedure above allowed the ratio of the intensities of the beams illuminating the object and reference pinhole to be the same for the two configurations. However, for a fair comparison it is also necessary to use the same absolute intensities for the two geometries. With $N = 1$, the detected harmonic fluence was larger by a factor of 3.125 than in the $N = 2$ beam case, in part due to the spatial chirp imparted onto the beam by the shaping process. This was accounted for by increasing the pulse energy and adjusting the CCD exposure time for the $N = 1$ case to be $3.125^{-1} = 0.32$ times that required for the $N = 2$ case.

We subsequently plot results against normalised exposure times where the normalisation factors for the $N = 1$ and $N = 2$ beam experiments are 0.32 and 1 respectively. This allows the comparison of results where the total harmonic flux incident upon on the sample is equivalent.

In this work it was possible to increase the exposure times in the N=1 case to achieve a S:N in the detected hologram comparable to the N=2 case. However, this will not always be possible since sample vibration and pointing drift in the illumination will in general reduce the visibility of the detected interference fringes and hence the S:N in the recovered image. It is therefore desirable to develop methods for increasing fringe visibility whilst retaining short exposure times.

7. Results

Figure 6(a) and 6(b) show the detected holograms recovered for the cases of $N = 1$ and $N = 2$ beams for a normalized exposure times of 120, corresponding to 38.4 and 120 seconds respectively, in accordance with the constraints of section 6. When plotted on a log scale, the hologram shown in Fig. 6(b) has visible interference fringes up to the outer limits of the CCD chip, corresponding to locations containing high spatial frequencies. Figures 6(c) and 6(d) show that the object is recovered in both the $N = 1$ and $N = 2$ cases, but in the $N = 2$ case the recovered image is less noisy and exhibits a superior S:N. The $N = 1$ image has a more uniform intensity in the transparent regions of the object which results from the more uniform illumination provided by the larger beam used in this case.

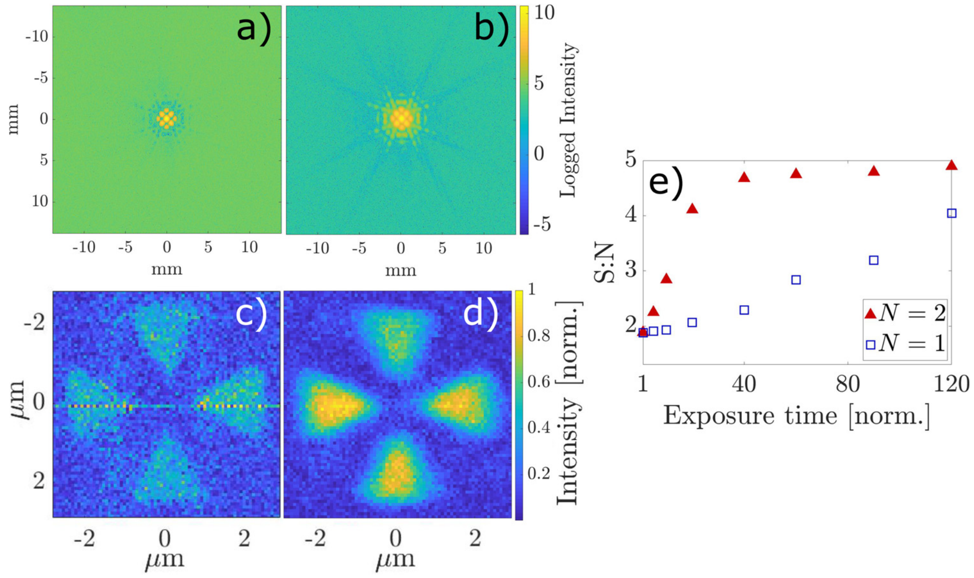

Fig. 6. Detected holograms on a log scale for normalised exposures of 120 for $N = 1$ (a) and $N = 2$ (b) beams. Recovered images for normalised exposures of 120 for $N = 1$ (c) and $N = 2$ (d) beams. e) Variation of the S:N ratio as a function of normalized exposure time for the case of $N = 1$ (open blue squares) and $N = 2$ (full red triangles) beams.

To calculate the S:N of the images, the image signal is taken to be the pixel values in Figs. 6(c) and 6(d) within the area of the object found by performing a similarity transformation of the SEM image onto the retrieved images. The background is taken as the remaining pixels values not included in the image signal. Figure 6(e) shows the calculated S:N as a function of normalised exposure time for the cases of $N = 1$ and $N = 2$, within the constraints described in section 6. It can be seen that the S:N of the recovered image is larger, and increases with normalized exposure time more quickly, when the sample is illuminated by $N = 2$ beams.

Fourier ring correlation [40] curves were calculated for the data presented in Figs. 6(a) and 6(b). Resolutions of 580 nm and 420 nm were found for ring correlation thresholds of 0.5 and 0.143 [41]. These values are consistent with the expected resolution limit in an FTH image of approximately 70% of the reference diameter [33]. The diameters of the reference pinholes used in this experiment were roughly 490 nm.

8. Conclusions and outlook

To conclude, we have presented a method for the programmable and independent manipulation of the relative positions and intensities of multiple harmonic beams. The potential advantages of this method were demonstrated by FTH imaging of an object with two, independently-controllable HHG beams. It was found that FTH imaging with two HHG beams yielded reconstructed images with superior S:N than equivalent imaging with a single beam.

Pending the next generation of higher damage threshold liquid crystal on silicon adaptive optics [42], the number of HHG beams that can be generated with our method is restricted. The throughput of the beamline in Fig. 1(a) is limited by the damage threshold of the SLM to approximately 1 W for 1 kHz repetition rate 30 fs duration laser pulses. For harmonic generation to occur, the peak intensity of each beamlet must exceed a threshold of approximately $1\text{x}10^{14}\,\text{Wcm}^{-2}$ and with our available power and focussing geometry, two harmonic beams could be generated. Tighter focusing would allow the generation of more harmonic beams, the maximum number being limited by a requirement that the Rayleigh range of the driver foci must be larger than the thickness of the gas cell. Alternatively, static bespoke phase plates with higher damage thresholds could be used to generate an increased number of harmonic beams albeit at the expense of flexibility.

Within the field of imaging, multi-beam ptychography [43,44] and blind digital holography [45] in the XUV would benefit greatly from the use of multiple harmonic beams. High resolution images could be obtained at a fraction of typical exposure times, mitigating limitations of stability in long exposure experiments. In addition, the maturity of high harmonic sources has led to an abundance of experiments that would benefit from multiple, controlled XUV beams [27,28,46]. Beyond imaging, techniques ranging from high harmonic metrology [19] to interferometry [18] would benefit from the control provided by our method.

The work described here paves the way for new classes of experiments enabled by the ability to generate multiple, independently controlled harmonic beams.

Funding

Engineering and Physical Sciences Research Council (EP/L015137/1, EP/N029313/1); H2020 Marie Skłodowska-Curie Actions (641272).

Acknowledgments

The author would like to thank Dr Jason Brown for assistance with sample fabrication and Mr Rick Makin for the sample coating. The authors declare that they have no competing financial interests.

References

1. M. B. Gaarde, J. L. Tate, and K. J. Schafer, "Macroscopic aspects of attosecond pulse generation," J. Phys. B: At., Mol. Opt. Phys. **41**(13), 132001 (2008).

2. L. He, Q. Zhang, P. Lan, W. Cao, X. Zhu, C. Zhai, F. Wang, W. Shi, M. Li, X. Bian, P. Lu, and A. D. Bandrauk, "Monitoring ultrafast vibrational dynamics of isotopic molecules with frequency modulation of high-order harmonics," Nat. Commun. **9**(1), 1108 (2018).
3. J. C. Petersen, S. Kaiser, N. Dean, A. Simoncig, H. Y. Liu, A. L. Cavalieri, C. Cacho, I. C. E. Turcu, E. Springate, F. Frassetto, L. Poletto, S. S. Dhesi, H. Berger, and A. Cavalleri, "Clocking the melting transition of charge and lattice order in 1t-tas$_2$ with ultrafast extreme-ultraviolet angle-resolved photoemission spectroscopy," Phys. Rev. Lett. **107**(17), 177402 (2011).
4. D. Azoury, O. Kneller, S. Rozen, B. D. Bruner, A. Clergerie, Y. Mairesse, B. Fabre, B. Pons, N. Dudovich, and M. Krüger, "Electronic wavefunctions probed by all-optical attosecond interferometry," Nat. Photonics **13**(1), 54–59 (2019).
5. M. E. Couprie, "New generation of light sources: Present and future," J. Electron Spectrosc. Relat. Phenom. **196**, 3–13 (2014).
6. F. Weise, D. M. Neumark, S. R. Leone, and O. Gessner, "Differential near-edge coherent diffractive imaging using a femtosecond high-harmonic xuv light source," Opt. Express **20**(24), 26167–26175 (2012).
7. E. L. Falcão-Filho, C.-J. Lai, K.-H. Hong, V.-M. Gkortsas, S.-W. Huang, L.-J. Chen, and F. X. Kärtner, "Scaling of high-order harmonic efficiencies with visible wavelength drivers: A route to efficient extreme ultraviolet sources," Appl. Phys. Lett. **97**(6), 061107 (2010).
8. A. Ozawa, J. Rauschenberger, C. Gohle, M. Herrmann, D. R. Walker, V. Pervak, A. Fernandez, R. Graf, A. Apolonski, R. Holzwarth, F. Krausz, T. W. Hänsch, and T. Udem, "High harmonic frequency combs for high resolution spectroscopy," Phys. Rev. Lett. **100**(25), 253901 (2008).
9. T. Popmintchev and M.-C. Chen, "Phase matching of high harmonic generation in the soft and hard X-ray regions of the spectrum," Proc. Natl. Acad. Sci. U. S. A. **106**(26), 10516–10521 (2009).
10. F. Wiegandt, P. N. Anderson, F. Yu, D. J. Treacher, D. T. Lloyd, P. J. Mosley, S. M. Hooker, and I. A. Walmsley, "Quasi-phase-matched high-harmonic generation in gas-filled hollow-core photonic crystal fiber," Optica **6**(4), 442–447 (2019).
11. K. O'Keeffe, D. Lloyd, and S. Hooker, "Quasi-phase-matched high-order harmonic generation using tunable pulse trains," Opt. Express **22**(7), 7722–7732 (2014).
12. S. Hädrich, J. Rothhardt, M. Krebs, F. Tavella, A. Willner, J. Limpert, and A. Tünnermann, "High harmonic generation by novel fiber amplifier based sources," Opt. Express **18**(19), 20242–20250 (2010).
13. P. Jaeglé, *Coherent Sources of XUV Radiation: Soft X-Ray Lasers and High-Order Harmonic Generation*, Springer Series in Optical Sciences (Springer, New York, 2007).
14. Q. Huang, M. de Boer, J. Barreaux, R. van der Meer, E. Louis, and F. Bijkerk, "High efficiency structured EUV multilayer mirror for spectral filtering of long wavelengths," Opt. Express **22**(16), 19365–19374 (2014).
15. H. Pan, C. Späth, A. Guggenmos, S. H. Chew, J. Schmidt, Q. zhong Zhao, and U. Kleineberg, "Low chromatic fresnel lens for broadband attosecond xuv pulse applications," Opt. Express **24**(15), 16788–16798 (2016).
16. Y. Wang, W. Yun, and C. Jacobsen, "Achromatic fresnel optics for wideband extreme-ultraviolet and x-ray imaging," Nature **424**(6944), 50–53 (2003).
17. E. Louis, A. Yakshin, T. Tsarfati, and F. Bijkerk, "Nanometer interface and materials control for multilayer euv-optical applications," Prog. Surf. Sci. **86**(11-12), 255–294 (2011).
18. L. Jian, E. F. Cunningham, Y. S. You, D. A. Reis, and S. Ghimire, "Interferometry of dipole phase in high harmonics from solids," Nat. Photonics **13**(2), 96–100 (2019).
19. M. Bellini, C. Lyngå, A. Tozzi, M. B. Gaarde, T. W. Hänsch, A. L'Huillier, and C.-G. Wahlström, "Temporal coherence of ultrashort high-order harmonic pulses," Phys. Rev. Lett. **81**(2), 297–300 (1998).
20. J.-F. Hergott, T. Auguste, P. Salières, L. L. Déroff, P. Monot, P. d'Oliveira, D. Campo, H. Merdji, and B. Carré, "Application of frequency-domain interferometry in the extreme-ultraviolet range by use of high-order harmonics," J. Opt. Soc. Am. B **20**(1), 171–181 (2003).
21. Y. H. Jiang, T. Pfeifer, A. Rudenko, O. Herrwerth, L. Foucar, M. Kurka, M. Lezius, and M. F. Kling, "Temporal coherence effects in multiple ionization of N 2 via XUV pump-probe autocorrelation," Phys. Rev. A **82**(4), 041403 (2010).
22. G. Genoud, O. Guilbaud, E. Mengotti, S.-G. Pettersson, E. Georgiadou, E. Pourtal, C.-G. Wahlström, and A. L'Huillier, "Xuv digital in-line holography using high-order harmonics," Appl. Phys. B: Lasers Opt. **90**(3-4), 533–538 (2008).
23. R. L. Sandberg, A. Paul, D. A. Raymondson, S. Hädrich, D. M. Gaudiosi, J. Holtsnider, R. I. Tobey, O. Cohen, M. M. Murnane, H. C. Kapteyn, C. Song, J. Miao, Y. Liu, and F. Salmassi, "Lensless diffractive imaging using tabletop coherent high-harmonic soft-x-ray beams," Phys. Rev. Lett. **99**(9), 098103 (2007).
24. A.-S. Morlens, J. Gautier, G. Rey, P. Zeitoun, J.-P. Caumes, M. Kos-Rosset, H. Merdji, S. Kazamias, K. Cassou, and M. Fajardo, "Submicrometer digital in-line holographic microscopy at 32 nm with high-order harmonics," Opt. Lett. **31**(21), 3095–3097 (2006).
25. I. McNulty, J. Kirz, C. Jacobsen, E. H. Anderson, M. R. Howells, and D. P. Kern, "High-resolution imaging by fourier transform x-ray holography," Science **256**(5059), 1009–1012 (1992).
26. G. K. Tadesse, W. Eschen, R. Klas, V. Hilbert, D. Schelle, A. Nathanael, M. Zilk, M. Steinert, F. Schrempel, T. Pertsch, A. Tünnermann, J. Limpert, and J. Rothhardt, "High resolution XUV Fourier transform holography on a table top," Sci. Rep. **8**(1), 8677 (2018).

27. J. Duarte, “Coherent xuv imaging,” Ph.D. thesis, Tecnico Lisboa (2015).
28. G. O. Williams, A. I. Gonzalez, S. Künzel, L. Li, M. Lozano, E. Oliva, B. Iwan, S. Daboussi, W. Boutu, H. Merdji, M. Fajardo, and P. Zeitoun, “Fourier transform holography with high harmonic spectra for attosecond imaging applications,” Opt. Lett. **40**(13), 3205 (2015).
29. M. Guizar-Sicairos and J. R. Fienup, “Holography with extended reference by autocorrelation linear differential operation,” Opt. Express **15**(26), 17592–17612 (2007).
30. H. Pettersson, *The Encyclopaedia of Medical Imaging* (Isis Medical Media, 1998).
31. J. Goodman, *Statistical Optics*, A Wiley-Interscience publication (Wiley, 1985).
32. D. Skoog, F. Holler, and S. Crouch, *Principles of Instrumental Analysis* (Thomson Brooks/Cole, 2007).
33. W. F. Schlotter, “Lensless fourier transform holography with soft x-rays,” Ph.D. thesis, Stanford University (2007).
34. W. F. Schlotter, R. Rick, K. Chen, A. Scherz, J. Stöhr, J. Lüning, S. Eisebitt, C. Günther, W. Eberhardt, O. Hellwig, and I. McNulty, “Multiple reference Fourier transform holography with soft x rays,” Appl. Phys. Lett. **89**(16), 163112 (2006).
35. B. Henke, E. Gullikson, and J. Davis, “X-ray interactions: photoabsorption, scattering, transmission, and reflection at E=50-30000 eV, Z=1-92,” At. Data Nucl. Data Tables **54**(2), 181–342 (1993).
36. F. Dickey and T. Lizotte, *Laser Beam Shaping Applications*, Optical Science and Engineering (CRC Press, 2017).
37. Y. Qin, T. Nakajima, H. Zen, X. Wang, T. Kii, and H. Ohgaki, “Characterization of non-Gaussian mid-infrared free-electron laser beams by the knife-edge method,” Infrared Phys. Technol. **66**, 146–151 (2014).
38. L. Andrews, *Special Functions of Mathematics for Engineers*, Oxford science publications. (SPIE Optical Engineering Press, 1998). Page 110.
39. T. Poon and J. Liu, *Introduction to Modern Digital Holography: With Matlab* (Cambridge University, 2014).
40. R. P. J. Nieuwenhuizen, K. A. Lidke, M. Bates, D. L. Puig, D. Grünwald, S. Stallinga, and B. Rieger, “Measuring image resolution in optical nanoscopy,” Nat. Methods **10**(6), 557–562 (2013).
41. W. O. Saxton and W. Baumeister, “The correlation averaging of a regularly arranged bacterial cell envelope protein,” J. Microsc. **127**(2), 127–138 (1982).
42. G. Xia, W. Fan, D. Huang, H. Cheng, J. Guo, and X. Wang, “High damage threshold liquid crystal binary mask for laser beam shaping,” High Power Laser Sci. Eng. **7**, e9 (2019).
43. X. Pan, C. Liu, and J. Zhu, “Single shot ptychographical iterative engine based on multi-beam illumination,” Appl. Phys. Lett. **103**(17), 171105 (2013).
44. P. Sidorenko and O. Cohen, “Single-shot ptychography,” Optica **3**(1), 9 (2016).
45. P. Anderson, F. Wiegandt, D. Treacher, M. Mang, I. Gianani, A. Schiavi, D. Lloyd, K. O’Keeffe, S. Hooker, and I. Walmsley, “Blind digital holographic microscopy,” Proc. SPIE **10127**, 101270H (2017).
46. R. L. Sandberg, D. A. Raymondson, C. La-o-vorakiat, A. Paul, K. S. Raines, J. Miao, M. M. Murnane, H. C. Kapteyn, and W. F. Schlotter, “Tabletop soft-x-ray fourier transform holography with 50 nm resolution,” Opt. Lett. **34**(11), 1618–1620 (2009).